



HAL
open science

Clay mineral evolution and formation of intermediate phases during pedogenesis on picrite basalt bedrock under temperate conditions (Yunnan, southwestern China)

Hanlie Hong, Kaipeng Ji, Hetang Hei, Chaowen Wang, Chen Liu, Lulu Zhao, Bruno Lanson, Chenlei Zhao, Qian Fang, Thomas Algeo

► To cite this version:

Hanlie Hong, Kaipeng Ji, Hetang Hei, Chaowen Wang, Chen Liu, et al.. Clay mineral evolution and formation of intermediate phases during pedogenesis on picrite basalt bedrock under temperate conditions (Yunnan, southwestern China). *CATENA*, 2023, 220, pp.106677. 10.1016/j.catena.2022.106677. insu-03833532

HAL Id: insu-03833532

<https://insu.hal.science/insu-03833532>

Submitted on 28 Oct 2022

HAL is a multi-disciplinary open access archive for the deposit and dissemination of scientific research documents, whether they are published or not. The documents may come from teaching and research institutions in France or abroad, or from public or private research centers.

L'archive ouverte pluridisciplinaire **HAL**, est destinée au dépôt et à la diffusion de documents scientifiques de niveau recherche, publiés ou non, émanant des établissements d'enseignement et de recherche français ou étrangers, des laboratoires publics ou privés.

1 **Clay mineral evolution and formation of intermediate phases during**
2 **pedogenesis on picrite basalt bedrock under temperate conditions**
3 **(Yunnan, southwestern China)**

4
5 Hanlie Hong^{1,2*}, Kaipeng Ji¹, Hetang Hei³, Chaowen Wang⁴, Chen Liu¹, Lulu Zhao¹,
6 Bruno Lanson⁵, Chenlei Zhao¹, Qian Fang¹, Thomas J. Algeo^{1,6,7}

7
8 ¹State Key Laboratory of Biogeology and Environmental Geology, China University of
9 Geosciences, Wuhan 430074, China

10 ²School of Earth Sciences, China University of Geosciences, Wuhan, Hubei, 430074, China

11 ³Yunnan Earthquake Agency, Kunming, Yunnan, 650224, China

12 ⁴Gemmological Institute, China University of Geosciences, Wuhan, Hubei, 430074, China

13 ⁵Univerisity of Grenoble Alpes, ISTERre, F-38041 Grenoble, France

14 ⁶Department of Geology, University of Cincinnati, Cincinnati, OH 45221-0013, USA

15 ⁷ State Key Laboratory of Geological Processes and Mineral Resources, China University of
16 Geosciences, Wuhan, Hubei 430074, China

17
18 **Abstract**

19 In order to better understanding clay mineral evolution coupled with geochemical
20 changes during weathering of igneous rocks under temperate conditions, the picrite
21 basalt-derived soil in Dali (South China) was investigated using X-ray diffraction
22 (XRD), X-ray fluorescence (XRF), scanning electron microscope (SEM), and

23 high-resolution transmission electron microscopy (HRTEM) methods. Our results
24 show that smectite and mixed-layer clays occur throughout the weathered soil profile,
25 while discrete kaolinite and illite phases are absent in the soil. From saprolite to
26 topsoil, smectite decreases sharply, while mixed-layer kaolinite/smectite (K/S) and
27 illite/smectite (I/S) clays increase markedly. Clay minerals in the saprolite consist of
28 both dioctahedral and trioctahedral species, while those of the middle to upper profile
29 display a uniform dioctahedral structure. I/S phases are characterized by
30 interstratification of 12-Å smectite and 10-Å illite layers, and K/S phases by
31 interstratification of 12-Å smectite and 7-Å kaolinite layers, with I/S/K clays
32 containing all three layer types. Kaolinization of smectite occurs at the initial stage of
33 weathering, earlier than that of smectite illitization. Desilication and K-fixation of
34 smectite take place simultaneously during advanced weathering, resulting in
35 formation of illitic and kaolinitic phases continuously throughout the developmental
36 history of the soil. Notably high K concentrations in the weathering profile may be
37 related to K-fixing in the interlayer of illite due to smectite illitization in response to
38 more advanced weathering and pedogenic processes, while the increasing K content
39 in the topsoil may be ascribed to fertilizer in land use and uptake of K by plants from
40 deeper soil horizons. Fe₂O₃ and TiO₂ accumulation in the topsoil is probably mediated
41 by microorganisms.

42

43 **Keywords:** kaolinite/smectite (K/S); illite/smectite (I/S); desilication; weathering;
44 soil formation; saprolite

45

46 **1. Introduction**

47 During weathering and pedogenesis, the initial alteration of basic igneous rocks
48 usually produces smectite, allophane, and imogolite in various environments, which
49 are then transformed into other clay phases, dominated by kaolins and mixed-layer
50 kaolinite/smectite (K/S), as soil formation proceeds (Alexander and Heal, 1974;
51 Kantor and Schwertmann, 1974; Curtin and Smillie, 1981; Glassmann and Simonson,
52 1985; Righi et al., 1999; Vingiani et al., 2004; Rasmussen et al., 2010; Perez-Fodich
53 and Derry, 2019). Neoformed smectite has a dioctahedral structure typically of a
54 ferriferous member of the montmorillonite-beidellite series, occurring in the lower
55 soil horizon, while illite and poorly-crystalline kaolinite predominate in the upper soil
56 profile (Kantor and Schwertmann, 1974; Curtin and Smillie, 1981).

57 Key weathering processes, such as acid hydrolysis and oxidation of bedrock as well
58 as the formation of secondary clay phases, are dependent on bedrock lithology and
59 other soil-forming factors such as climate, topography, and drainage conditions
60 (Chesworth, 1973; Curi and Franzmeier, 1987; Vingiani et al., 2004; Deepthy and
61 Balakrishnan, 2005; Li et al., 2016; Wilson et al., 2017; Perez-Fodich and Derry,
62 2019). Cool and moist climatic conditions favor the formation of short-range order
63 phases, whereas warm and dry conditions produce smectite, kaolins, and crystalline
64 Fe-oxyhydroxides (Dekayir and El-Maataoui, 2001; Rasmussen et al., 2010; Jiang et
65 al., 2018). Under humid temperate conditions at Killundine, Morvern, Scotland,
66 weathering of fresh basalt initially formed a trioctahedral clay phase that transformed

67 through a mixture of di- and trioctahedral species to a dioctahedral interstratified
68 illite/smectite (I/S) phase with minor hematite and anatase in highly weathered soils
69 (Bain, et al., 1980). In the temperate Middle Atlas, Morocco, weathering of alkali
70 basalt was initially dominated by dissolution of glass and deposition of
71 poorly-crystalline Si-Al products, which then transformed into halloysite, kaolinite,
72 and hematite during enhanced weathering, while illite and vermiculite were regarded
73 as introduced phases that did not originate from the basalt bedrock (Dekayir and
74 El-Maataoui, 2001). A basalt weathering under seasonally wet, temperate climate
75 conditions in Sardinia, Italy yielded mainly K/S clays, with drainage conditions
76 controlling the proportion of kaolinite in the mixed phase (Righi et al., 1999; Vingiani
77 et al., 2004). Also, the ferric smectite layer content in the K/S decreased upward
78 through the soil profile, and kaolinization of smectite took place by complete
79 dissolution of preferentially ferric smectite layers and crystallization of kaolinite
80 layers in the interlayer regions of smectite particles (Curtin and Smillie, 1981; Righi
81 et al., 1999). However, Singer and Armannsson (1999) reported that, in the
82 weathering profile of Pleistocene basalts under moderately humid Mediterranean
83 conditions, smectite was the only clay mineral formed in the saprolite, and the clay
84 fractions of the regolith consisted of smectite, kaolinite, and minor halloysite without
85 intermediate phases.

86 Various patterns and processes of pedogenesis in basic igneous rocks have also
87 been proposed (e.g., Bain, et al., 1980; Ma et al., 1999; Dekayir and El-Maataoui,
88 2001; Campodonico et al., 2019; Sulieman et al., 2020). Orhan and Hüseyin (2018)

89 showed that, in a subhumid climate, basalt-derived soils contained dominantly
90 smectite, with minor illite, kaolinite, and vermiculite, and the content of smectite
91 increased with depth in the soil and was controlled by local topography and drainage.
92 Under a temperate Mediterranean-type climate, weathering of basalts produced
93 dominantly smectite with minor kaolin, illite, and palygorskite at lower elevations,
94 whilst kaolin was dominant on local topographic highs (Prudêncio et al., 2002).
95 However, variation in the clay phases of basalt-derived soils has also been attributed
96 to other factors such as hydrothermal alteration during lava cooling (Bain et al., 1980;
97 Pokrovsky et al., 2005), illitization of smectite due to plant uptake of K from deeper
98 soil horizons (He et al., 2008), and influx of allochthonous aeolian material (Dekayir
99 and El-Maataoui, 2001; Rasmussen et al., 2010). Furthermore, Nesbitt and Wilson
100 (1992) claimed that climate conditions affect only the rates but not the mechanisms of
101 chemical weathering of basalts, and that the diversity of clay mineral assemblages
102 formed in basalt-derived soils under a range of climate conditions depends mainly on
103 the steady-state conditions of the climate regime (i.e., chemical weathering vs
104 erosion).

105 Although the weathering of basalt under temperate climate conditions seems to
106 conform to a general pattern of initial formation of smectite and subsequent
107 transformation toward kaolin (Prudêncio et al., 2002), the specific processes of basalt
108 pedogenesis and, especially, the characterization of intermediate phases in
109 basalt-derived soils remain a matter of debate (Bain, et al., 1980; Glassmann and
110 Simonson, 1985; Dekayir and El-Maataoui, 2001; Vingiani et al., 2004; He et al.,

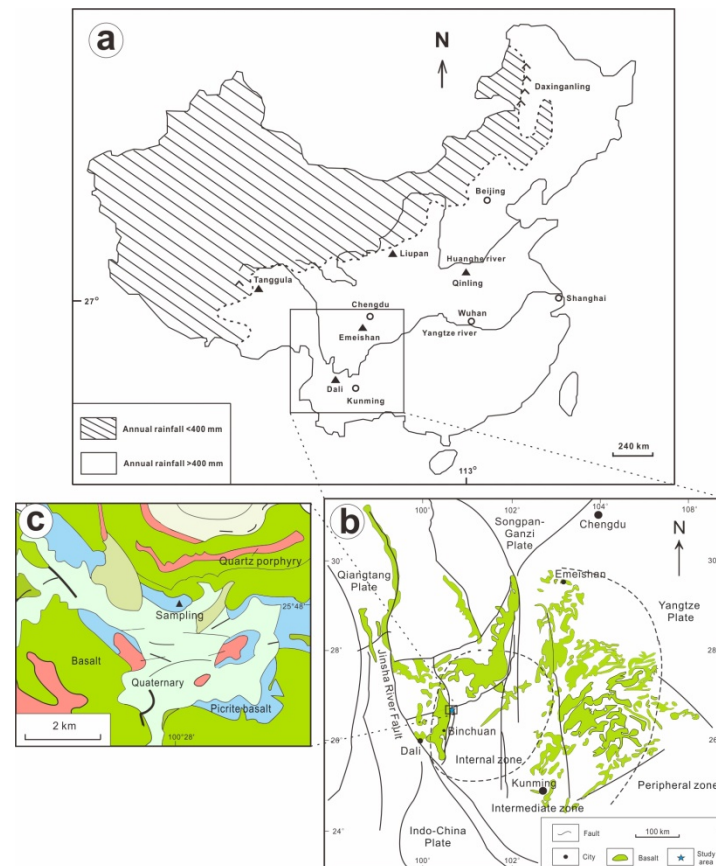
111 2008; Caner et al., 2014; Wilson et al., 2017; Jiang et al., 2018; Perez-Fodich and
112 Derry, 2019; Sulieman et al., 2020). A lack of investigation of the mineralogy of
113 picrite basalts undergoing weathering hinders a comprehensive understanding of the
114 evolution of clay phases and the transformative processes in such pedogenic systems.
115 Temperate climate conditions commonly allow development of a complete, advanced
116 sequence of intermediate weathering phases (Bain, et al., 1980; Vingiani et al., 2004).
117 In this study, analysis of the clay mineralogy and geochemical changes in a soil
118 profile developed on the well-studied basaltic bedrock in the temperate Dali region of
119 Yunnan Province, South China was undertaken in order to address the pattern of
120 pedogenesis and soil mineral evolution during weathering of picrite basalt. The aims
121 of our investigation were: (1) to provide new insights into the pedogenesis of picrite
122 basalt under temperate climate conditions, and (2) to provide additional constraints on
123 reaction pathways for formation of intermediate clay-mineral phases during
124 weathering.

125

126 **2. Study area**

127 The study area is situated in the central zone of the Emeishan Large Igneous Province,
128 in the southwestern part of the Yunnan-Guizhou Plateau, southwestern China (Fig. 1).
129 The Emeishan basaltic traps, with a cumulative thickness ranging from five
130 kilometers (proximally) to tens of meters (distally), are part of a major large igneous
131 province outcropping mainly in southwestern China over an area in excess of a
132 quarter million square kilometers with a center near Dali (Yunnan) to Miyi (Sichuan)

133 (He et al., 2003). They overlie Late Permian carbonates of the Maokou Formation and
 134 are overlain by the Triassic Wujiaping sedimentary sequence (Courtilot et al., 1999;
 135 He et al., 2003). The lithology of the Emeishan traps changes slightly as a function of
 136 local tectonic setting, occurring as basalt, picrite basalt, alkaline basalt, tholeiite, and
 137 minor picrate, trachyandesite, and trachyte (Hou et al., 1999).



138
 139 Fig. 1. Location and geologic setting. (a) Climate map showing mean annual precipitation in
 140 China; (b) Regional geological map showing the distribution of the Emeishan Large Igneous
 141 Province; (c) Detail of study area.

142 The landscape of the Dali area consists of plateaus, mountains, and intermontane
 143 basins, including geomorphic units representing high mountain canyons, alluvial fans,
 144 lakeside slopes, broad valleys, and complex terrains, at altitudes ranging from 1340 to
 145 4122 m above sea level. It has a low-latitude plateau monsoonal climate characterized

146 by a mean annual temperature of 15.1 °C (mean monthly temperatures range from 3.7
147 to 28.9 °C) and a mean annual precipitation of ~700 mm. The study section is located
148 at Daying town (100°28'E, 25°48'N), Dali City, Yunnan Province, South China, at an
149 altitude of 1722 m. Eolian sediments have not been observed in Dali, as monsoonal
150 winds transport eolian materials only as far southward as the middle of China (Qiao et
151 al., 2011). The vegetation of the study area consists dominantly of alpine herbs and
152 the high-altitude shrubs belonging to the genus *Quercus*, and human land use is
153 constrained mainly to maize cultivation owing to the limited rainfall. Soil developed
154 at the footslope position, where excavation for a water channel provided access to a
155 4.6-m-thick soil profile overlying unweathered picrite basalt bedrock.

156 3. Materials and methods

157 3.1. Field sampling

158 The topsoil (Layer 1, 0-40 cm) displays a porous and loose crumb structure and is
159 brownish gray in color, consisting mainly of sandy clays and minor gravels, with
160 relatively abundant organic matter and plant roots. A reddish-brown silty clay horizon
161 (Layer 2, 40-100 cm) is present under the topsoil, exhibiting a homogeneous crumb
162 structure and containing minor plant roots. The underlying horizon (Layer 3, 100-160
163 cm) is light gray in color and blocky in structure, having short white clay veins or
164 spots. A thick grayish-brown clayey gravel saprolite horizon (Layer 4, 160-380 cm) is
165 present beneath Layer 3. It is composed dominantly of clays and gravels of
166 incompletely weathered bedrock, with minor amounts of Fe-Mn nodules. The bedrock
167 is greyish-green picrite basalt that exhibits an amygdaloidal structure (Fig. 2).

168 Representative samples (~1 kg each) were collected from the weathering profile at
169 10-20 cm intervals in the upper portion (0-1.6 m) and at 40 cm intervals in the
170 saprolite (1.6-3.8 m) of the lower portion, yielding a total of 18 samples.



171
172 Fig. 2. Photographs of the Dali weathering soil profile developed on picrite basalt. (a) A full view
173 of the soil profile. (b), (c), (d), (e), and (f) are close-up photographs showing Layers 1, 2, 3, 4,
174 and the bedrock, respectively. Scale provided by 13-cm-long marker.

175 3.2. Selected chemical and mineralogical analyses

176 Soil pH measurements were performed in distilled water using a glass electrode in
177 a 1:2.5 soil/water suspension. The cation exchange capacity (CEC) determination of

178 soil samples was performed using the sodium chloride–ethanol method of [Chen et al.](#)
179 [\(2000\)](#). For total organic carbon (TOC) analysis, the soil samples were ground to pass
180 through a 200-mesh sieve. The powdered samples were then reacted with
181 hydrochloric acid ($0.1 \text{ mol}\cdot\text{L}^{-1}$) overnight to remove carbonate. TOC measurement
182 was performed on a Vario Macro Cube carbon analyzer. For X-ray diffraction (XRD)
183 analysis, whole-rock samples were air-dried at $60 \text{ }^{\circ}\text{C}$ overnight and then ground
184 manually to powder using an agate mortar and pestle. The mineral contents of the
185 whole-rock samples were estimated using the reference intensity ratio approach with
186 admixture of corundum as the internal standard ([Hillier, 2000](#)). The mixing powder
187 samples were prepared by mounting the powders into sample holders using a
188 back-press technique. The characteristic peaks of minerals used in our calculation
189 were 3.34 \AA (quartz), 3.19 \AA (plagioclase), 3.51 \AA (anatase), 2.97 \AA (clinopyroxene),
190 2.90 \AA (pumpellyite), and 2.70 \AA (hematite), 15 \AA (smectite), and 7.40 \AA
191 (kaolinite/smectite), respectively. The relative standard deviation of the
192 semi-quantitative method is usually $< 15 \%$.

193 The clay fraction ($< 2 \text{ }\mu\text{m}$) was extracted using the sedimentation method ([Jackson,](#)
194 [1978](#)), and an oriented clay-fraction sample was prepared for clay mineralogical
195 investigation by pipetting the clay suspension, with a solid-to-liquid ratio of around
196 1:25, onto a glass slide that was subsequently air-dried at ambient temperature. In
197 order to determine swelling clay components, the oriented clay samples were treated
198 with ethylene glycol in a sealed glass desiccator heated at $65 \text{ }^{\circ}\text{C}$ for 4 h in an
199 electronic oven. XRD analysis was performed on a Panalytical XPert PRO DY2198

200 diffractometer with Ni-filtered Cu K α radiation. The instrument was operated at 40
201 kV tube voltage and 35 mA tube current conditions, with the slit system of 1°
202 divergence slit, 1° anti-scatter slit, and 0.3 mm receiving slit, and the XRD patterns
203 were collected from 3° to 65° 2 θ at a scan rate of 4° 2 θ min⁻¹ and a step size of 0.02°
204 2 θ .

205 For observation of the (060) peak of clay phases, the non-oriented clay samples
206 were prepared using the back-press method. The layer content of the end member in a
207 mixed-layer clay phase and the relative abundance of clay phases in the sample were
208 estimated using the NEWMOD II program (Reynolds and Reynolds, 1996), which
209 was performed simultaneously for the XRD patterns of both glycolated and
210 Ca-saturated clay samples.

211

212 *3.3. Major element compositions and mass balance calculations*

213 The chemical compositions of the samples were measured using X-ray fluorescence
214 (XRF). Prior to preparation of the fused XRF pellets, measurement of loss-on-ignition
215 (LOI) was performed by drying a sample aliquot in an oven at 105 °C for 2 h and then
216 heating 1 g of the dried sample to 1000 °C for 1.5 h. The LOI value was calculated
217 from the difference in weight between the sample aliquots heated to 105 °C and to
218 1000 °C. Preparation of fused pellets for XRF measurement was as follows: a 5-g
219 aliquot of sample was dried in an electronic oven at 60 °C overnight and then
220 manually ground to a fine powder with a grain size of less than 0.074 μ m (200 mesh)
221 for generation of fused XRF pellets. Major element compositions were analyzed on an

222 XRF-1800 SHIMADZU sequential X-ray fluorescence spectrometer. The detection
223 limit was generally ~0.01 wt%, and the relative standard deviation was usually < 1%.

224 The degree of mobilization of each element in the weathering profile was estimated
225 through a mass balance calculation using Al as an immobile reference element
226 (Campodonico et al., 2019) and the chemical composition of the unaltered bedrock as
227 the starting mass. The formula for this calculation is: $C_{GL} = [C_S / Al_S] \times Al_{BR} - C_{BR}$,
228 where C_{GL} , C_S , and C_{BR} represent the gain or loss (GL) of the element of interest as
229 well as its concentration in the soil sample (S) and the unaltered bedrock (BR), and
230 Al_S and Al_{BR} represent the aluminum concentrations of the sample and bedrock,
231 respectively.

232

233 3.4. SEM and HRTEM observations

234 Small chips (~1 cm) of whole-rock samples were selected and then gold-coated.
235 Scanning electron microscope (SEM) observation was undertaken on a Hitachi
236 SU8010 field emission scanning electron microscope, equipped with an Octane Super
237 X-ray energy-dispersive (EDS). The instrument was operated at an accelerating
238 voltage of 20 kV and a probe current of 2 nA, with a magnification up to 8×10^5 and a
239 resolution of secondary electron image of 1.0 nm.

240 For high resolution transmission electron microscope (HRTEM) observation, the
241 air-dried clay fraction was immersed in methanol solution and then ultrasonically
242 dispersed for 10 min, after which the clay material was collected with a copper net
243 and dried under an infrared light. HRTEM observation was performed on a Tecnai G2

244 20 S-TWIN high-resolution transmission electron microscope, equipped with a
245 GENESIS 2000 X-ray energy-dispersive (EDS). The instrument was operated at the
246 condition of 160 kV accelerating voltage, with a beam spot size of 1.5 nm, a point
247 resolution of 0.24 nm, and a line resolution of 0.14 nm.

248

249 **3. Results**

250 The pH, TOC, and CEC values of the soil samples are listed in [Table 1](#). The XRD
251 patterns of representative soil samples are shown in [Fig. 3a](#) and their mineral
252 compositions are tabulated in [Table 1](#). The clay mineral components and their relative
253 proportions were obtained from fitting XRD traces of the glycolated samples ([Fig. 4](#)),
254 and were further confirmed by fitting the air-dried samples ([Fig. 5](#)), and their relative
255 contents are listed in [Table 2](#).

256 *3.1. Physical and chemical properties and mineral compositions of the soil*

257 Mineral components in the soil profile are mainly clay minerals, plagioclase,
258 quartz, and hematite. Mineral abundances displayed only small changes between
259 samples from the same soil horizon but varied considerably between samples from
260 different soil layers, as reflected by intensities of their characteristic peaks of the
261 minerals ([Fig. 3a](#)). The bedrock consists dominantly of pumpellyite (2.90, 3.79, 4.67,
262 2.74, 2.52 Å) and clay minerals (15.0 Å), with minor amounts of plagioclase (3.18 Å),
263 quartz (3.34, 4.26, 1.82 Å), and hematite (2.70, 2.52, 1.485 Å) and trace
264 clinopyroxenes (2.97 Å), suggesting that the picrite basalt bedrock has undergone
265 low-grade burial metamorphism. In addition, the XRD profiles of selected

266 clay-fraction samples show that clay phases from the middle to upper soil profile
267 exhibit a uniform dioctahedral structure (1.50 Å), whereas those from the saprolite
268 horizon consist of both di- (1.50 Å) and trioctahedral (1.54 Å) species (Fig. 3b).

269 Clay species in the Dali soil profile are dominantly smectite, K/S, and I/S,
270 characterized by the 14.8 Å peak in the XRD patterns of the untreated whole-rock
271 samples (Fig. 3), which expanded to around 17 Å after glycolation (Figs. 4-5).
272 Smectite accounts for the 17-Å peak, and the notable decrease in intensity upward in
273 the soil profile indicates a gradual decrease in smectite content. I/S accounts for the
274 bump peak at ~8.5-8.8° 2θ, which is evident for the upper samples but not visible for
275 the deeper samples, indicating an upward increase of this mineral phase. The 7.4-Å
276 peak (~12° 2θ) is ascribed to a K/S phase with no contribution from discrete kaolinite,
277 which requires two sub-populations to be fitted properly since it is a broad reflection
278 (Table 2). K/S occurs throughout the soil profile, forming two sub-populations
279 marked by higher proportions and lower proportions of kaolinite layers, while I/S
280 occurs dominantly in Layers 1, 2, and 3 but is almost absent in the Layer 4. Overall,
281 smectite decreases concurrently with increases in I/S clays upward within the soil
282 profile, and K/S clays are notably less abundant in the lower samples relative to the
283 upper samples (Table 2).

284

285 3.2. Geochemical composition of the soil

286 The Dali soil shows marked variations in geochemical composition among its
287 component soil layers, but only small differences between samples from the same

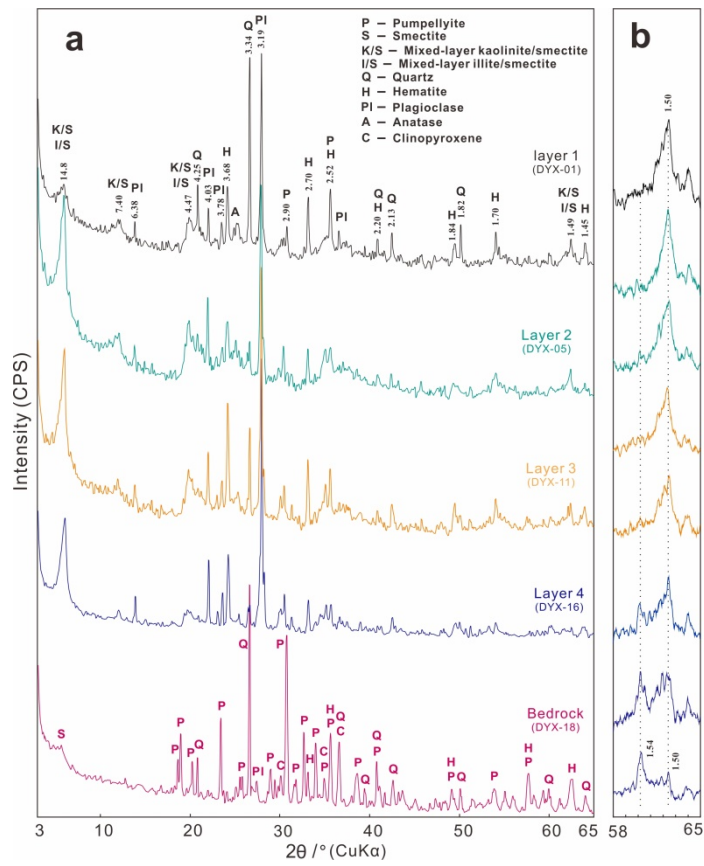
288 horizon (Table 3; Fig. 6). Samples from the lower profile, especially the Layer 4,
289 contain relatively more SiO₂ (49.6–51.7%) compared to those from the upper profile
290 (43.0–46.8%). TiO₂ contents are notably high (3.5–3.6%) in the Layer 1. Al₂O₃ is
291 modestly concentrated in the middle profile (Layers 2 and 3; 19.0-23.5%) relative to

292 Table 1. Some selected morphological, physical and chemical attributes, and mineral compositions of the soil developed from Dali picrite basalt weathering

Soil layer	Sample	Color	Texture	Structure	pH	TOC (wt%)	CEC (cmol(+)/kg)	Mineral content (wt%)						
								Clays	Pl	Qtz	Ant	Cln	Hm	Pum
Layer 1	DYX-01	5 YR5/1	Sandy clay	Crumb	4.9	1.64	24.3	50	17	7	3	2	16	5
Layer 2	DYX-05	5 YR5/6	Silty clay	Crumb	5.7	1.07	54.7	65	18	2	2	3	10	/
Layer 3	DYX-11	7.5 YR8/1	Clay	Blocky	6.0	0.59	34.5	57	19	5	2	6	11	/
Layer 4	DYX-16	7.5 YR6/2	Clayey gravel	Blocky	6.8	0.83	41.1	54	23	2	2	5	14	/
Bedrock	DYX-18	Grayish green	/	/	/	/	/	13	2	24	2	7	8	44

293 Notes: Pl-plagioclase; Qtz-quartz; Cln-clinopyroxene; Pum-pumpellyite; Hm-hematite; Ant-anatase; “/”-not measured or not detected.

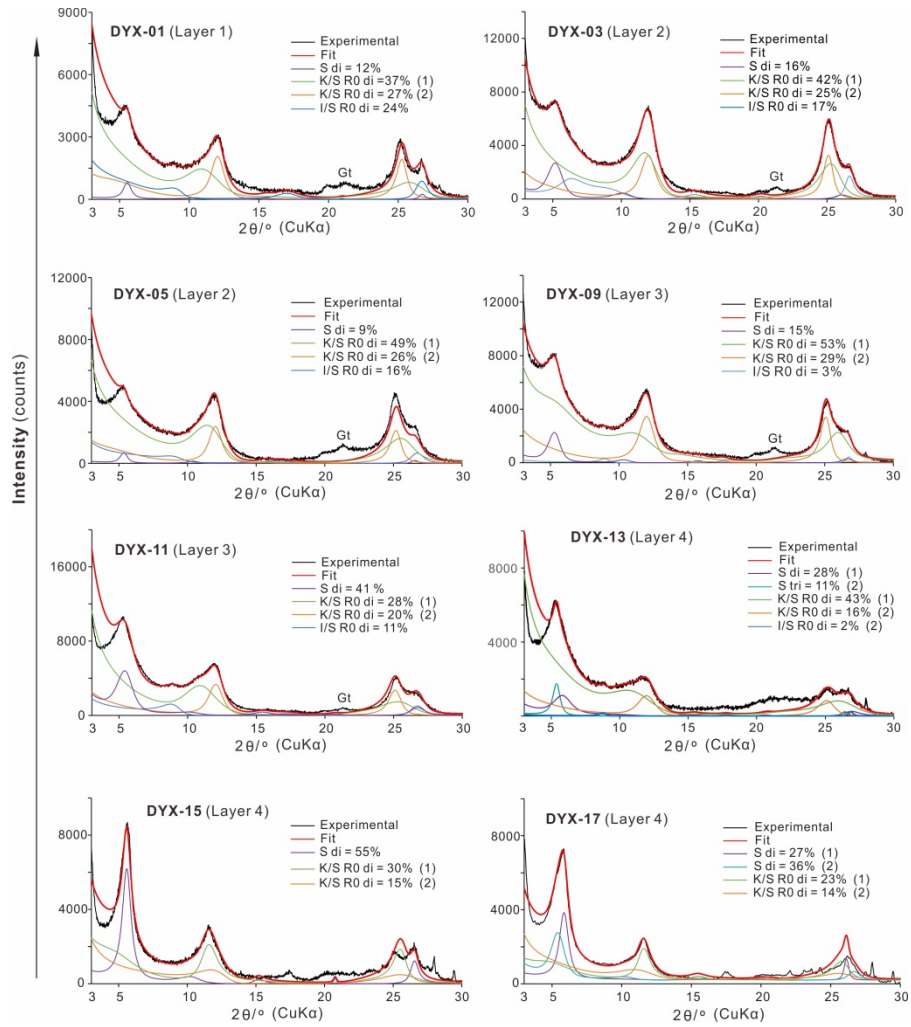
294



296

297 Fig. 3. XRD patterns of representative samples of the Dali soil profile. (a) Whole-rock samples; (b)

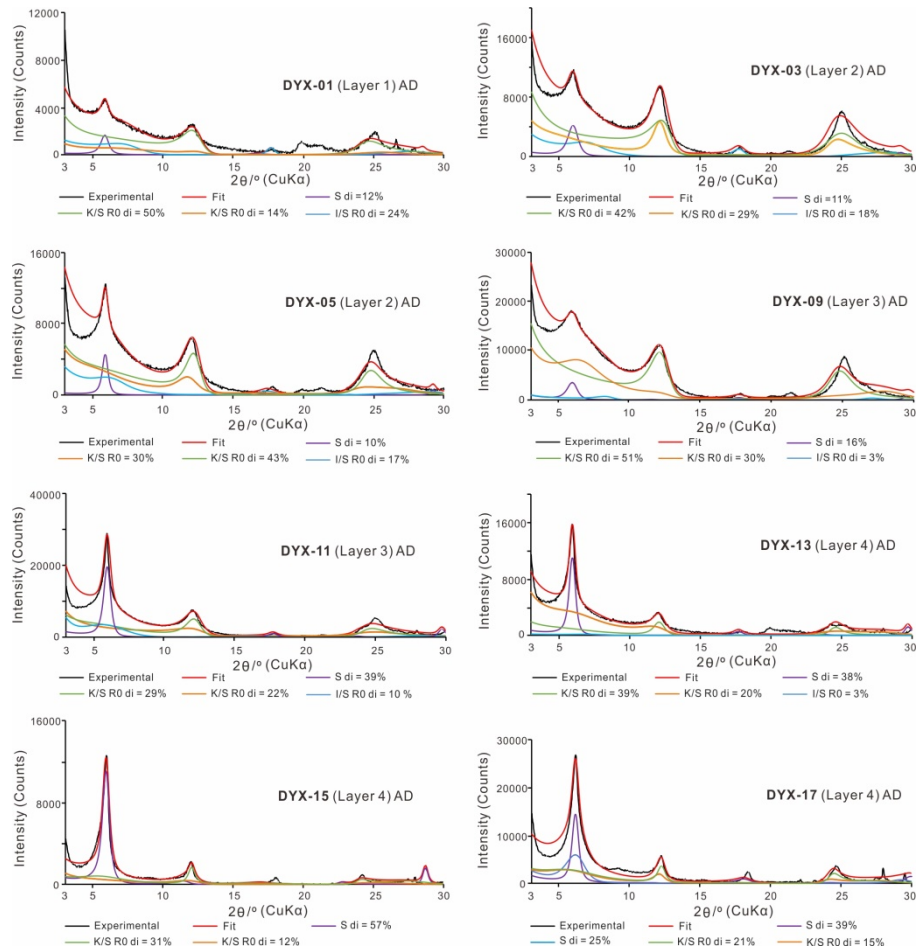
298 (060) reflections of XRD patterns of clay fractions.



299

300 Fig. 4. Fitted XRD patterns of glycolated clay fractions showing the stacking structures of
 301 mixed-layer clay species and their relative contents. Abbreviations: K/S: mixed-layer
 302 kaolinite/smectite; I/S: mixed-layer illite/smectite; S: smectite; Gt: goethite; di: dioctahedral;
 303 tri: trioctahedral.

304



305

306 Fig. 5. Fitted XRD patterns of air-dried clay fractions showing compatible clay mineral
 307 compositions to those of the glycolated samples (Fig. 4).

308

309 Table 2. Clay mineral compositions of representative soil samples from the Dali picrite basalt
 310 weathering profile (wt%)

Soil layer	Sample	Smectite	I/S (Illite layer content)	K/S (1) (Kaolinite layer content)	K/S (2) (Kaolinite layer content)	Total K/S
Layer 1	DYX-01	12	24 (79%)	37 (75%)	27 (87%)	64
Layer 2	DYX-03	16	17 (33%)	42 (86%)	25 (89%)	67
	DYX-05	9	16 (71%)	49 (82%)	26 (89%)	75
Layer 3	DYX-09	15	3 (90%)	53 (63%)	29 (90%)	82
	DYX-11	41	11 (85%)	28 (87%)	20 (92%)	48
Layer 4	DYX-13	39 (28 di+11 tri)	2 (93%)	43 (69%)	16 (87%)	59
	DYX-15	55 (33 di+22 tri)	/	30 (78%)	15 (84%)	45
	DYX-17	64 (22 di+42 tri)	/	23 (75%)	13 (77%)	36

311

Notes: I/S: mixed-layer illite/smectite; K/S: mixed-layer kaolinite/smectite, (1) relatively weak

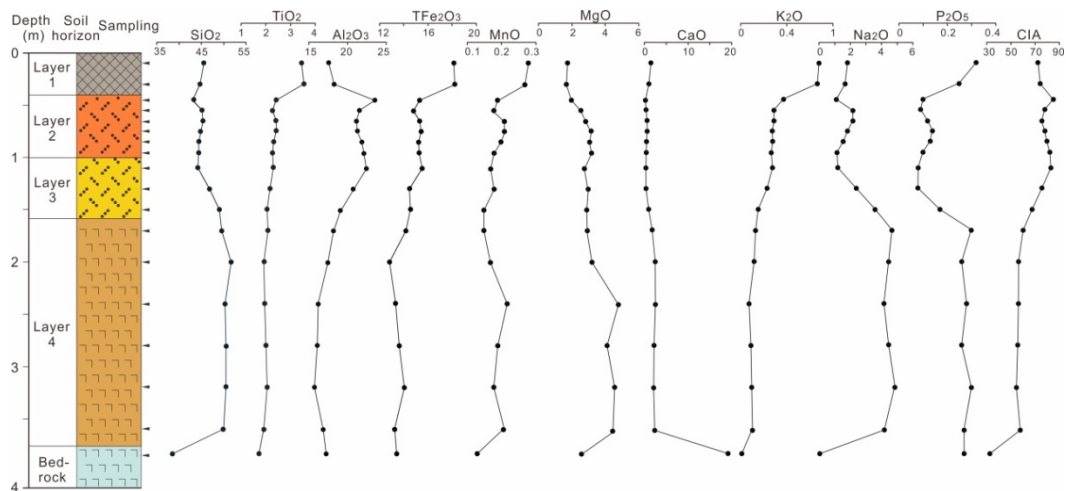
312

kaolinitization and (2) relatively strong kaolinitization; “/”: undetected; di: dioctahedral; tri:

313

trioctahedral.

314 Layer 1, Layer 4, and bedrock (15.6–18.2%). TFe_2O_3 is highest in Layer 1
 315 (18.1-18.2%), with intermediate and uniform values in Layers 2 and 3 (15.5%) and
 316 relatively lower values in the lower profile (Layer 4, 12.8-14.2%; bedrock, 11.9%).
 317 The MgO and CaO contents exhibit downward increases from 1.7 to 4.8% and from
 318 1.1 to 3.3%, respectively. Moreover, the CaO content of the bedrock is extremely high
 319 (to 19.5%). The Na_2O content of the soil samples shows a downward increase from
 320 1.1 to 4.8%, whereas the K_2O content exhibits a downward decrease from 0.9 to 0.1%.
 321 However, the Na_2O and K_2O contents of the bedrock are markedly lower (0.02% and
 322 0.01%, respectively). The P_2O_5 content of the soil samples varies from 0.1 to 0.3%,
 323 but Layer 1 and Layer 4 contain generally more P_2O_5 relative to the other soil layers.



324
 325 Fig. 6. Changes in major element contents (wt%) and CIA through the Dali picrite basalt weathering
 326 soil profile.

327

328 3.3. SEM observations

329 In general, clay flakes in Layer 1 display a relatively smooth and flat basal (001)
 330 plane and exhibit a generally poorly-developed pseudo-hexagonal or plate-like outline
 331 (Fig. 7a). Also, the edges of clay mineral flakes are relatively straight, similar to the
 332 common morphologies of kaolinite and illite. Clay mineral grains in Layer 2 often

333

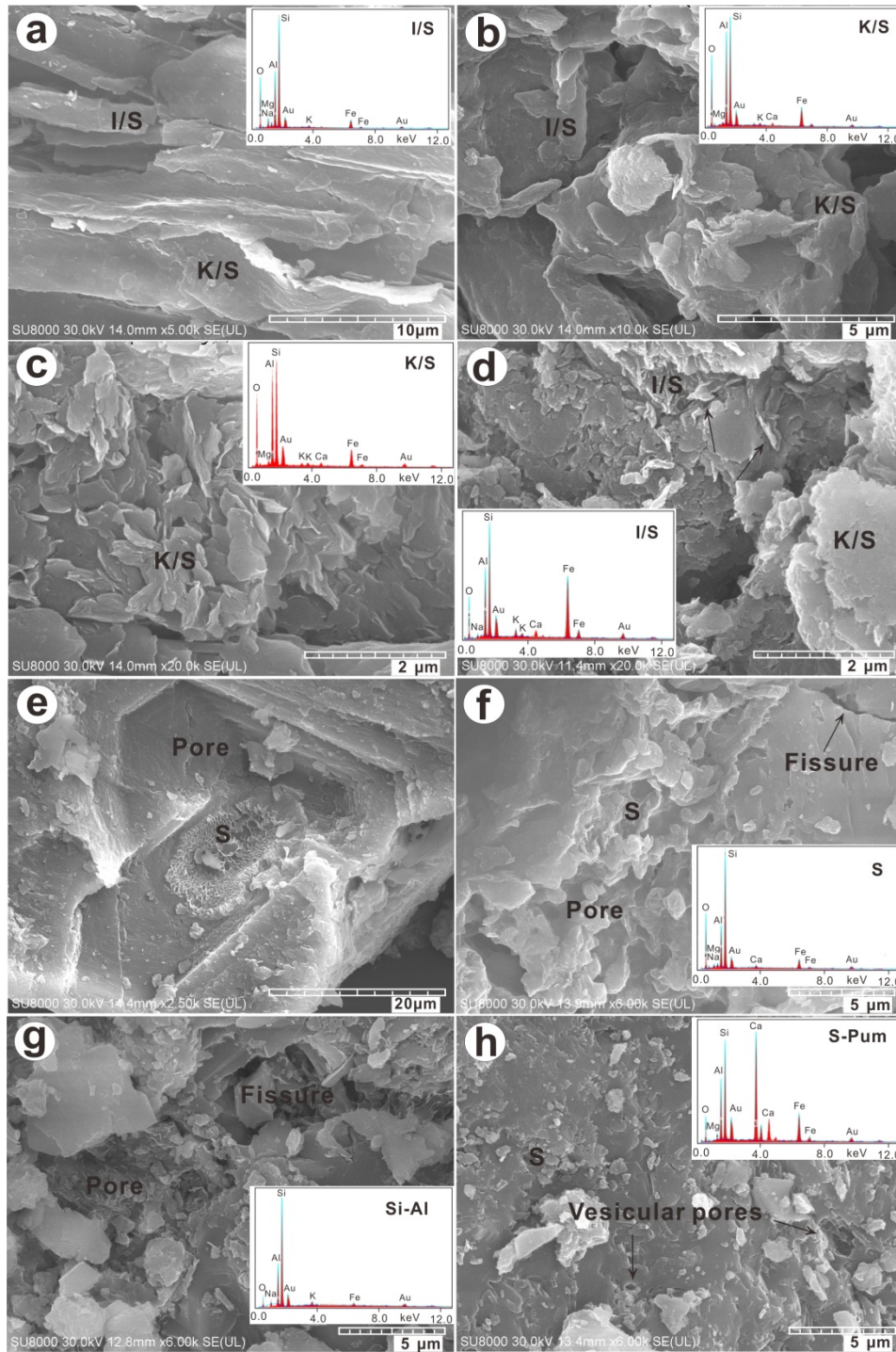
334

Table 3. Major element chemistry and CIA and MIA indices of alteration of soil samples from the Dali picrite basalt weathering profile (wt%)

Soil layer	Sample number	SiO ₂	TiO ₂	Al ₂ O ₃	TFe ₂ O ₃	MnO	MgO	CaO	Na ₂ O	K ₂ O	P ₂ O ₅	LOI	SUM	CIA	MIA	Zr (10 ⁻⁶)	TiO ₂ / Al ₂ O ₃	Zr/TiO ₂
Layer 1 (0-40 cm)	DYX-01	45.59	3.47	17.50	18.15	0.28	1.75	2.30	1.81	0.85	0.32	7.63	99.65	72	44	388	0.198	0.011
	DYX-02	44.73	3.56	18.22	18.22	0.27	1.66	1.90	1.66	0.83	0.25	8.21	99.52	74	48	376	0.195	0.011
Layer 2 (40-100 cm)	DYX-03	43.03	2.43	23.50	15.32	0.19	1.97	1.06	1.06	0.46	0.10	10.74	99.84	85	71	257	0.103	0.011
	DYX-04	45.14	2.29	21.50	14.81	0.18	2.54	1.20	2.16	0.36	0.09	9.19	99.45	78	56	236	0.107	0.010
	DYX-05	45.30	2.43	21.11	15.33	0.21	2.82	1.45	2.16	0.36	0.12	8.91	100.20	76	52	245	0.115	0.010
	DYX-06	44.90	2.44	21.23	15.44	0.21	3.17	1.48	1.82	0.34	0.14	9.16	100.24	78	56	232	0.115	0.010
	DYX-07	44.36	2.34	21.85	15.25	0.20	3.08	1.32	1.58	0.35	0.13	9.60	100.05	80	60	228	0.107	0.010
	DYX-08	44.37	2.29	22.07	15.26	0.18	3.17	1.21	1.15	0.33	0.10	9.95	100.07	83	68	222	0.104	0.010
Layer 3 (100-160 cm)	DYX-09	44.19	2.32	22.42	15.54	0.17	2.74	1.10	1.19	0.35	0.08	10.10	100.21	84	68	227	0.103	0.010
	DYX-10	46.77	2.18	20.66	14.49	0.18	3.01	1.22	2.42	0.29	0.08	8.55	99.86	76	52	212	0.106	0.010
	DYX-11	49.06	2.06	19.02	14.58	0.15	2.88	1.75	3.57	0.19	0.17	6.74	100.16	67	35	194	0.108	0.009
Layer 4 (160-380 cm)	DYX-12	49.60	2.10	18.15	14.18	0.15	2.94	2.57	4.70	0.16	0.30	5.17	100.01	59	18	184	0.116	0.009
	DYX-13	51.66	1.94	17.42	12.82	0.17	3.21	3.25	4.45	0.15	0.26	4.81	100.14	56	13	170	0.111	0.009
	DYX-14	50.29	1.97	16.16	13.35	0.22	4.79	3.29	4.16	0.09	0.28	5.26	99.85	56	11	166	0.122	0.008
	DYX-15	50.45	2.01	16.02	13.62	0.19	4.11	3.03	4.46	0.11	0.26	5.04	99.30	55	11	171	0.125	0.009
	DYX-16	50.54	2.06	15.64	14.06	0.18	4.56	2.92	4.84	0.12	0.30	4.74	99.96	54	8	171	0.132	0.008
	DYX-17	49.95	1.94	16.85	13.28	0.21	4.45	3.00	4.18	0.13	0.27	5.51	99.78	57	15	388	0.115	0.008
Bedrock	DYX-18	41.73	1.74	16.58	11.86	0.12	2.40	19.51	0.02	0.01	0.29	5.20	99.44	32		376	0.105	0.008

335

Notes: LOI is loss on ignition; CIA = $(Al_2O_3 / (Al_2O_3 + CaO* + K_2O + Na_2O)) \times 100\%$; MIA = $2 \times (CIA - 50)$; Fe in all Fe₂O₃



336

337 Fig. 7. SEM images of the Dali samples. (a) Poorly-developed pseudo-hexagonal and plate-like
 338 grains indicating presence of K/S and I/S ($\text{SiO}_2/\text{Al}_2\text{O}_3$ value of 1.74) clays in Layer 1
 339 (DYX-01); (b) Relatively well-crystalline K/S ($\text{SiO}_2/\text{Al}_2\text{O}_3$ value of 1.23) and I/S clay
 340 minerals in Layer 2 (DYX-05); (c) K/S clays ($\text{SiO}_2/\text{Al}_2\text{O}_3$ value of 1.25) with curled edges
 341 indicating relatively weak kaolinization in the Layer 3 (DYX-09); (d) K/S and I/S
 342 ($\text{SiO}_2/\text{Al}_2\text{O}_3$ value of 1.65) clays with ragged outlines confined by basalt grains showing

343 replacement by clay minerals, and I/S clays with curled edges in pores indicating clay
344 formation in free spaces in Layer 4 (DYX-16); (e),(f),(g) Typical honeycombed polygonal
345 smectite ($\text{SiO}_2/\text{Al}_2\text{O}_3$ value of 2.96) in pore space indicating crystallization from porewater
346 solution in Layer 4 (DYX-16), and fissures and pores in the bedrocks and some of them
347 filling with Si-Al aggregates ($\text{SiO}_2/\text{Al}_2\text{O}_3$ value of 3.12) as reflected by the EDS (DYX-18);
348 (h) Vesicular structure and poorly-developed fine-grained smectite associated pumpellyite
349 showing chemical compositions of mainly Si, Ca, Al, and Fe in the bedrock (DYX-18). (I/S:
350 mixed-layer illite/smectite; K/S: mixed-layer kaolinite/smectite; S: smectite; Pum:
351 pumpellyite).

352

353 exhibit relatively well-developed euhedral pseudo-hexagonal morphology with a
354 smoother basal (001) plane and straighter edges (Fig. 7b), indicating higher
355 crystallinity relative to those of the topsoil. In the Layer 3, although most of the clay
356 mineral grains display a relatively smooth basal (001) plane, clay minerals usually
357 develop curled edges and thus typically exhibit wave-shaped outlines (Fig. 7c),
358 consistent with the morphologies of typical K/S and I/S clays (Hong et al., 2008;
359 2017).

360 Clay minerals in the Layer 4 display three different morphologies: (1) Abundant
361 clay particles that are extremely small in comparison with those in the overlying soil
362 layers; they display ragged outlines (Fig. 7d) and often replace basalt particles. (2)
363 Clay minerals that are larger and typically develop curled edges in fissures or in the
364 interstitial spaces among residual basalt particles, suggesting the occurrence of
365 smectite or I/S clays (Fig. 7d). (3) Clay minerals with a honeycombed polygonal
366 pattern, indicative of neformed smectite (Fig. 7e); their distinctive curled edges and
367 interwoven structure, as well as their presence primarily in open cavities, are

368 suggestive of smectite that crystallized from solution during weathering. The picrite
369 basalt bedrock shows generally a solid glass structure, with only rare small vesicular
370 pores (Fig. 7f).

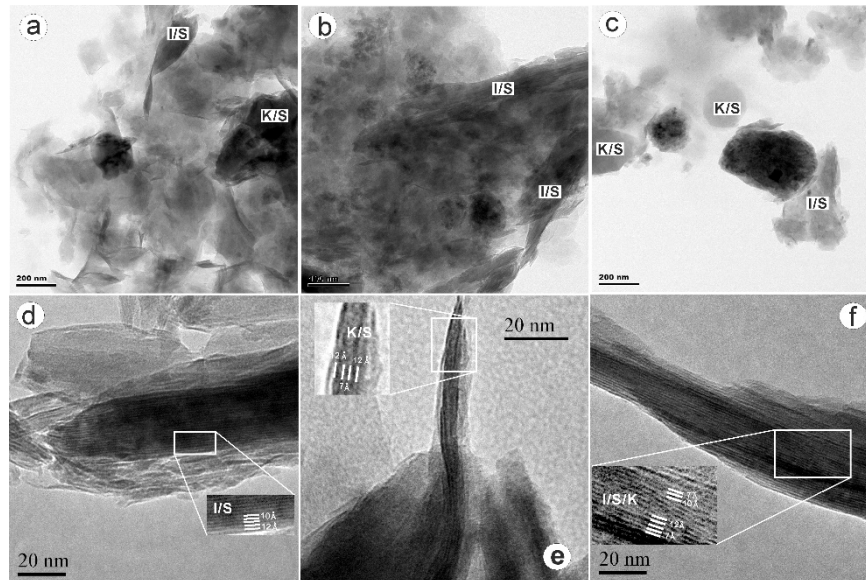
371

372 3.4. HRTEM observations

373 Clay particles generally display a wave-shaped morphology and have a relatively
374 thin and poorly developed (001) surface (Fig. 8a). The edges of these particles are
375 typically curved and curled, consistent with the characteristic morphologies of
376 smectite, K/S, and I/S clays (Van Der Gaast et al. 1986; Hong et al., 2012). However,
377 in samples from the upper soil profile, some of the clay flakes exhibit relatively
378 euhedral morphologies in long, plate-shaped crystals with straight outlines along the
379 (001) dimension, consistent with the crystal morphology of strongly illitized I/S clays
380 (Fig. 8b). Clay flakes with relatively well-developed euhedral pseudo-hexagonal
381 outlines are also present in these soil samples (Fig. 8c). The basal (001) planes of clay
382 particles are smooth and flat, and their lateral surfaces (110) and (010) are clearly
383 defined with straight edges, similar to the morphology of kaolinite.

384 The margins of clay particles with thick and lath-shaped morphologies usually
385 display straight lattice fringes with 10-Å spacing, in agreement with those of illite
386 layers. However, the 10-Å fringes are often intercalated with 12-Å smectite layers,
387 indicative of the presence of interstratified I/S (Fig. 8d). For clay particles with
388 relatively thin and wave-shaped morphology, the 12-Å fringes are often irregularly
389 interstratified with 7-Å fringes, suggesting the occurrence of K/S (Fig. 8e). In addition,

390 the 12-Å layers are occasionally observed to be interstratified with both 7-Å kaolinite
391 layers and 10-Å illite layers (Fig. 8f), indicating a mixed-layer smectite, illite, and
392 kaolinite (I/S/K) stacking structure.



393
394 Fig. 8. HRTEM observations showing the morphology and interstratified lattice fringes of clay
395 minerals of the Dali soil. (a) Wave-shaped morphology of K/S and I/S (DYX-13, Layer 4); (b)
396 An elongate and relatively straight morphology indicative of strong illitization of I/S
397 (DYX-13, Layer 4); (c) Euhedral pseudo-hexagonal outlines showing strong kaolinization of
398 K/S (DYX-5, Layer 2); (d) I/S clay with interstratified 12-, 10-, and 7-Å lattice fringes
399 (DYX-5, Layer 2); (e) K/S clay showing interstratification of 12-Å with 7-Å layer (DYX-13,
400 Layer 4); (f) Interstratified 12-, 10-, and 7-Å lattice fringes characteristic of mixed smectite,
401 illite, and kaolinite layers (I/S/K) (DYX-13, Layer 4).

402

403 4. Discussion

404 4.1. Clay mineral evolution through the weathering profile

405 As a result of burial metamorphism, the Dali picrite basalt bedrock consists mainly
406 of pumpellyite, smectites, hematite, quartz, and minor amounts of plagioclase,
407 clinopyroxenes, and anatase (Fig. 3; Table 2). The Emeishan basalts commonly

408 display amygdaloidal and vesicular structures (Hou et al., 1999). This volcanic rock
409 was subjected to burial diagenesis during the Late Permian, producing mainly
410 pumpellyite, smectite, and hematite (Mevel, 1981; Inoue and Utada, 1991; Mirabella
411 et al., 2005; De Rosa et al., 2016). The picrite basalt rock consists mainly of SiO₂,
412 FeO, MgO, CaO, Al₂O₃, corresponding to the general mineral compositions of olivine
413 and plagioclase. The burial alteration process can be described as the following
414 reaction equation: 3MgFeSiO₄ (olivine) + 5CaAlSi₂O₈ (plagioclase) + 12 H⁺ →
415 Ca₄MgAl₅[Si₂O₇]₂[SiO₄]₂(OH)₅·H₂O (pumpellyite) + CaMg₂[Si₄O₁₀](OH)₂·1.5H₂O
416 (smectite) + 1.5Fe₂O₃ (hematite) + 3SiO₂. Tectonic uplift has exposed the Emeishan
417 basalts, and supergene weathering has taken place since the Late Triassic. Initial
418 alteration of the bedrock entailed dissolution of pumpellyite (Table 3; Fig. 6),
419 followed by precipitation of newly formed smectite clays in small fissures and pores
420 in the bedrock (Fig. 7e,f,g). The poorly-crystalline small clay grains are often
421 replacements of pumpellyite aggregates as the latter alter into smectite (Fig. 7h).
422 Dissolution of bedrock in the first stage of weathering yielded relatively less mobile
423 Si-Al-rich materials in fissures and pores (Fig. 7g) and subsequently crystallized to
424 larger smectite flakes with curled edges in honeycombed polygonal aggregates (Fig.
425 7e,f).

426 Although smectite is typically the clay-mineral phase in thermodynamic
427 equilibrium with soil solutions during basalt weathering, microenvironmental
428 conditions can act as kinetic influences on clay-mineral evolution that yield different
429 products from thermodynamic predictions (Ziegler et al., 2003). Microenvironments

430 such as cavities and cracks favor rapid uptake of Al released by poorly-crystalline
431 Si-Al-rich materials (Fig. 7c) and thus facilitate smectite-to-kaolinite transformations.
432 At Dali, smectite is the dominant (39-64%) secondary clay species in the saprolite
433 horizon, but it decreases in the middle to upper soil profile due to transformation of
434 smectite to mixed-layer K/S. The limited transformation of smectite to I/S clay is
435 probably attributable to the low K content (0.01%) of the bedrock (Tables 2 and 3).
436 Well-drained conditions usually favor development of kaolinitic soils, whereas
437 poorly-drained environments formation of smectitic Vertisols (Kantor and
438 Schwertmann, 1974; May et al., 1986; Vingiani et al., 2004). In the Dali soil profile,
439 transformation of smectite to K/S and I/S clays was most common in pores (Fig. 7b, c,
440 d). The clay mineral assemblage of mixed-layer K/S and I/S clays, smectite, and
441 Fe-oxides, together with plagioclase and trace pumpellyite, suggests that smectite
442 layers experienced desilication and transformed preferentially to kaolinitic and illitic
443 phases (Glassmann and Simonson, 1985; Righi et al., 1999; Wilson et al., 2017).
444 However, the dominance of K/S and I/S clays in association with minor discrete
445 smectite, as well as a lack of discrete kaolinite and illite through the Dali soil profile,
446 is probably indicative of early-stage desilication within the soil (Figs. 3 and 4; Table
447 2). Also, the occurrence of plagioclase and absence of gibbsite at Dali confirm a low
448 weathering intensity due to limited acid leaching during basalt alteration, consistent
449 with its significantly low CIA values (Bakker et al., 1996; Vingiani et al., 2004; He et
450 al., 2008; Perez-Fodich and Derry, 2019).

451 Upward within the Dali soil profile, from Layer 4 to Layer 2, I/S and K/S clays

452 generally increase while smectite concurrently decreases, associated with increasing
453 proportions of illitic and kaolinitic layers in I/S and K/S clays, respectively (Table 2).
454 The intercalation of 12-Å smectite and 10-Å illite layers in I/S clays is indicative of
455 illitization of smectite due to K-fixation (Fig. 8d), and the random intercalation of
456 12-Å smectite and 7-Å kaolinite layers in clay particles suggests kaolinization of
457 smectite due to intense weathering (Fig. 8e). The interstratification of 12-Å smectite,
458 10-Å illite, and 7-Å kaolinite layers reflects formation of mixed-layer I/S/K clays (Fig.
459 8f), probably due to simultaneous transformation of smectite to illite and kaolinite as
460 weathering proceeded.

461 The upward decrease in smectite through the weathering profile is clearly due to
462 the kaolinization and illitization of this mineral during the weathering process (cf.
463 Orhan and Hüseyin, 2018). In wide climate conditions, smectite and smectitic
464 interstratifications are common clay mineral assemblages in basalt-derived soils (Bain,
465 et al., 1980; Eggleton et al., 1987; Righi et al., 1999; Vingiani et al., 2004; Barbera et
466 al., 2008; Perez-Fodich and Derry, 2019). In the Dali soil profile, the markedly higher
467 K/S content of Layer 2 and the upper Layer 3 compared to other soil layers (Table 2)
468 is consistent with their relatively greater penetrative condition in the soil profile, and
469 the presence of smectite, K/S, I/S, and I/K/S clays is attributable to relatively weak
470 chemical weathering under temperate, low-rainfall conditions. An increase in the
471 kaolinitic and illitic components of a soil usually causes a decrease in cation-exchange
472 capacity, since the CEC of a soil is dependent mainly on its clay content—especially
473 that of expandable phases (Bain et al., 1980; He et al., 2008; Babechuk et al., 2014).

474 The high CECs of the Dali soil (24.3-54.7 cmol/kg) agree well with the presence of
475 smectite, K/S, and I/S clays (Table 2). Unlike previously studied basalt weathering
476 profiles (e.g., Curtin and Smillie, 1981; Lessovaia et al., 2016; Van Ranst, et al., 2020),
477 clay mineral phases at Dali exhibit structural variation linked to weathering intensity:
478 the weakly weathered saprolite horizon is characterized by a mixture of di- and
479 trioctahedral species, whereas clays in the middle to upper profile have a more
480 uniform dioctahedral structure due to intense weathering (Fig. 3). These changes in
481 clay-mineral structure, which are associated with an increase of Al and a decrease of
482 Mg, probably reflect the replacement of Mg by Al and the oxidation of Fe²⁺ to Fe³⁺
483 during kaolinization and illitization of smectite in the upper part of the soil profile.

484 Although the mechanism of transformation of tri- and dioctahedral clay minerals to
485 dioctahedral mixed-layer clay minerals remains poorly understood, it is probably
486 associated with the alteration of smectite to kaolinite in the Dali soil (Righi et al.,
487 1999; Ryan and Huertas, 2009). The neoformed montmorillonite in the saprolite
488 horizon is dominated by migration of Ca and uptake of Mg and Fe (Christidis, 1998),
489 which results in the co-existence of both di- and trioctahedral species. As weathering
490 proceeds, the precursor of trioctahedral smectite becomes thermodynamically
491 unstable due to reduced Mg concentrations in the pore fluid and, especially, the more
492 acidic conditions in the middle to upper soil profile (Kittrick, 1973), resulting in
493 alteration of smectite to kaolinite and/or illite. This transformation is often considered
494 to be a solid-state process in which the tetrahedral sheets of smectite are stripped
495 away (Ryan and Huertas, 2009; Hong et al., 2012). Decomposition of the tetrahedral

496 sheets leads to a redistribution of elements marked primarily by the loss of Si and gain
497 of Al. In acidic conditions, Al from interlayer sites will be mobilized, and increasing
498 Al concentrations in the pore fluid will favor the diffusion of Al between external
499 solution and interlayer space of smectite and thus the replacement of octahedral Mg
500 by Al (Mavris et al., 2011; Cheng et al., 2022). In addition, Fe²⁺ in dioctahedral sites
501 of the parent mineral is likely to be oxidized to Fe³⁺ during transformation of smectite
502 to mixed-layer K/S, analogous to the oxidation of Fe²⁺ during transformation of
503 dioctahedral biotite to neoformed clay phases during early-stage weathering (Jeong
504 and Kim, 2003; Cheng et al., 2022).

505 Given the low K content of the picrite basalt bedrock, the notably higher K
506 concentrations in the Dali soil imply efficient retention by neoformed clay phases of
507 K released from the basalt through weathering. The increase in K content coupled
508 with an increase of illite in the upper soil profile suggests that K is incorporated in the
509 interlayer of illite due to smectite illitization in response to more advanced weathering
510 and pedogenic processes (Table 2). K enrichment of the topsoil has been widely
511 observed in weathering soil profiles developed on basalts elsewhere (e.g., Nesbitt and
512 Wilson, 1992; Sheldon, 2003; He et al., 2008), a phenomenon that has been attributed
513 to targeted uptake of K in the deeper soil by plants (Barré et al., 2007; He et al., 2008;
514 Bakker et al., 2019) or to the addition of K-rich aeolian material (Nesbitt and Wilson,
515 1992; Sheldon, 2003). In the Dali soil profile, the composition of the clay mineral
516 assemblage (i.e., presence of smectite, K/S, I/S, and I/S/K but absence of a mica-like
517 phase) strongly suggests an autochthonous weathering product. However, K-rich

518 aeolian material from the northern Tibetan Plateau is transported via monsoonal winds
519 only as far southward as the zone along the Yangtze River, far from the Dali area in
520 southern China (Qiao et al., 2011; Cheng et al., 2018). The relative accumulation of K
521 in the topsoil of the Dali profile may be ascribed to fertilizer in human land use of
522 mainly maize cultivation, as indicated by the notably higher TOC value, the distinctly
523 black color, and the sharp boundary between the underlying soil layer (Table 1; Fig. 2),
524 and also to the recycling uptake of K by plants from deeper soil horizons. These
525 processes result in K-fixing in illitic minerals and facilitate illitization of smectite,
526 consistent with much more illitic clays in the topsoil (He et al., 2008; Bakker et al.,
527 2019).

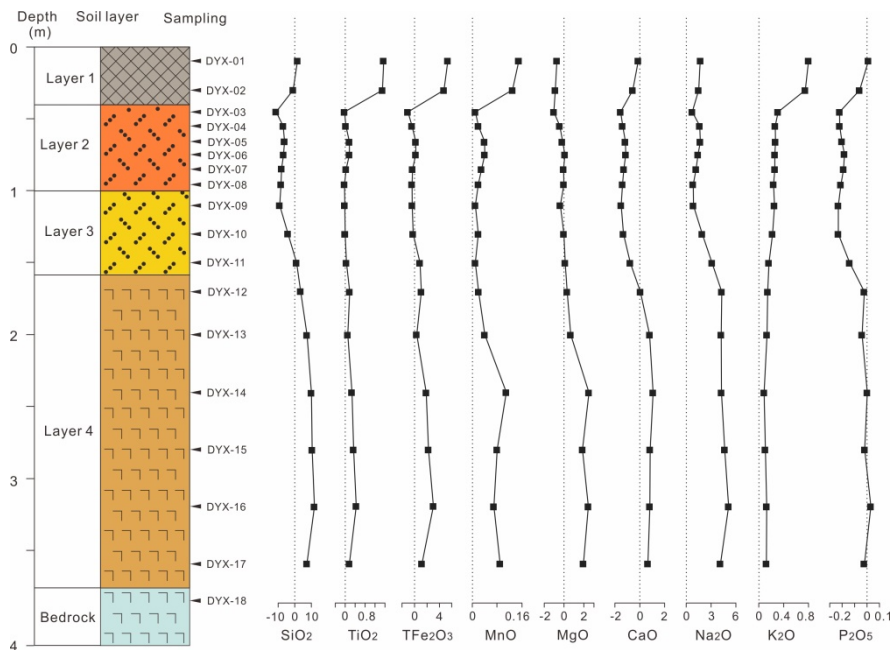
528

529 *4.2. Distribution of major elements in the basalt-derived soils*

530 Development of soil during weathering of basalts is generally accompanied by the
531 loss of mobile elements such as Si, Ca, and Mg, and by significant accumulation of
532 immobile elements such as Fe and Al (Chesworth et al., 1981; Eggleton et al., 1987;
533 Markússon and Stefánsson, 2011; Babechuk et al., 2014). Al is regarded as the most
534 immobile element during chemical weathering of volcanic materials (Chesworth et al.,
535 1981; Pokrovsky et al., 2005; Hong et al., 2019).

536 The major element oxides SiO₂, MgO, and CaO were gained in the Layer 4 and lost
537 from other soil layers at Dali. TiO₂ and TFe₂O₃ were gained throughout the soil
538 profile except for a few samples showing losses in Layers 2 and 3. MnO, Na₂O, and
539 K₂O were mostly gained, whereas P₂O₅ was generally lost during weathering (Fig. 9).

540



541

542

Fig. 9. Gain or loss of major elements through the Dali soil profile.

543

The notable accumulation of SiO₂ in Layer 4 was likely associated with chemical

544

weathering of altered picrite basalt bedrock, since weathering of fresh basalt is

545

generally characterized by dissolution of silicates and glass as well as the formation of

546

a poorly-crystalline Si-Al product (Daux et al., 1994; Dekayir and El-Maataoui, 2001).

547

Kaolinization and illitization of smectite is a desilication process, and the notable

548

decreases in Mg, Ca, and Mn in the upper profile were associated with the

549

transformation of tri- and dioctahedral clay minerals to dioctahedral clay species. The

550

strong depletions of SiO₂, CaO, and MgO in Layers 1, 2, and 3 at Dali were related to

551

abundant formation of advanced weathering phases, as the previously formed (i.e.,

552

early) weathering products transformed over time to thermodynamically more stable

553

phases such as K/S and I/S clays and well-crystalline Fe-oxyhydroxides (Glasmann

554

and Simonson, 1985; May et al., 1986; Righi et al., 1999; Liivamägi et al., 2018).

555

P₂O₅ displays a general decrease upwards, with depletion in Layers 2 and 3 that were

556 probably due to biogeochemical P cycling and/or leaching in view of the eluvial
557 condition and high TOC content of the soil (Wang et al., 2022).

558 Al_2O_3 , Fe_2O_3 , and TiO_2 show gradual increases upward through the Dali
559 weathering profile (Table 3; Figs. 6 and 9). The bedrock has a CIA value of 32, and
560 the soil profile shows a progressive change in CIA from 54 in Layer 4 to 85 in the
561 Layer 2, indicating a general upward increase in weathering intensity. However, the
562 gains or losses of Fe_2O_3 , MnO , and TiO_2 relative to Al_2O_3 are inconsistent with these
563 CIA values. Fe_2O_3 , MnO , and TiO_2 are markedly enriched in Layer 1 and Layer 4 but
564 relatively depleted in Layers 2 and 3 compared to Al_2O_3 . This indicates that, although
565 chemical weathering caused loss of mobile components and gain of immobile
566 components, the fluxes of Fe_2O_3 , MnO , and TiO_2 and their sites of concentration or
567 redistribution differed from those of Al_2O_3 .

568 The mineralogical index of alteration (MIA) is used to estimate the transformation
569 ratio of a primary mineral into its equivalent alteration mineral. MIA values of <20,
570 20-60, and >60 reflect incipient, intermediate, and intense to extreme mineralogical
571 transformations, respectively (Voicu et al., 1997). Layer 4 in the lower soil profile has
572 MIA of 8-18, consistent with the absence of K/S clays and the preservation of a
573 certain amount of pumpellyite (Fig. 3). Layers 1, 2, and 3 have notably higher MIA of
574 35 to 71, although only a few values are >60, corresponding to greater amounts of
575 K/S in those samples. This MIA pattern indicates a general upward increase in
576 weathering intensity and an intermediate degree of mineralogical alteration for the
577 Dali soil profile as a whole.

578 Similarly to the MIA index, the Dali soil profile exhibits dominantly incipient (CIA
579 = 50–60) to intermediate (CIA = 60–80) chemical weathering intensities, with only a
580 few samples in Layers 2 and 3 showing intense weathering (CIA > 80) (Table 3). The
581 moderate weathering intensities indicate that kaolinization did not go to completion,
582 consistent with clay mineral assemblages consisting mainly of K/S, smectite, and
583 minor I/S species (Caner et al., 2014; Van Ranst et al., 2020). The presence of
584 plagioclase also indicates relatively limited chemical weathering (Table 3; Fig. 3),
585 allowing preservation of certain labile elements (e.g., Ca, Mg, Na, and K) (Berry et al.,
586 1983; He et al., 2008). Although Na is largely retained within the soil profile, its
587 lower layers contain notably more Na₂O (3.57-4.84%) than its upper layers
588 (1.06-2.42%), indicating a degree of Na loss. Na exhibits a gain-or-loss trend that is
589 markedly similar to that of Ca (Fig. 6), indicating that their weathering behaviour is
590 strongly linked. Covariation of Na and Ca reflects a common provenance in
591 plagioclase, a mineral that is relatively well preserved in the lower soil profile where
592 the bedrock has undergone only incipient weathering. Similar upward decreases in Na
593 and Ca suggest their congruent removal due to chemical weathering of plagioclase in
594 the upper soil profile. In particular, all soil layers exhibit the same clay mineral
595 assemblage consisting of smectite and mixed-layer K/S and I/S clays, with K/S and
596 I/S clays increasing and smectite decreasing toward the top of the profile (Table 2; Fig.
597 4).

598 Zr and Ti are also considered to be the least mobile elements during weathering of
599 basalts (Eggleton et al., 1987; Nesbitt and Wilson, 1992; Arslan et al., 2006). At Dali,

600 soil samples from Layer 4 to Layer 1 have nearly uniform Zr/TiO₂ ratios of
601 0.008-0.011, indistinguishable from that of the basalt bedrock (0.008) (Table 3). This
602 observation suggests that the weathering profile represents mainly or exclusively *in*
603 *situ* weathering products, with little to no addition of allochthonous Fe- and K-rich
604 aeolian materials. However, the soil profile contains notably more K compared to its
605 bedrock (Fig. 9). The formation of pumpellyite and smectite in the bedrock suggests
606 that this igneous rock has experienced a hydrothermal alteration when buried by the
607 overlying Maokou Formation and the Wujiaping Formation (Mevel, 1981; Inoue and
608 Utada, 1991; Hou et al., 1999; He et al., 2003; Mirabella et al., 2005; De Rosa et al.,
609 2016). The notable more K in the soil profile is probably related to incorporation of K
610 by illite in response to more advanced weathering and pedogenic processes.

611 The immobile oxides TFe₂O₃ and TiO₂ are markedly enriched in the topsoil at
612 Dali (Fig. 9), consistent with the greater amounts of hematite and anatase in this layer
613 (Fig. 3). The concentration of these immobile components is often attributed to the
614 loss of mobile elements during intense weathering (Brantley et al., 2007;
615 Perez-Fodich and Derry, 2019). However, in iron-rich duricrusts in the tropical
616 regions of Brazil, the concentration of these immobile components may involve the
617 direct role of microorganisms (Levett et al. 2020). Microbial-induced weathering in
618 iron-rich duricrusts promotes the dissolution of iron, aluminum, and titanium oxide
619 minerals, allowing limited migration at a mineral scale before reprecipitation. Soluble
620 ferrous iron readily reprecipitates in the pore spaces in proximity to microorganisms
621 due to changes in oxidation potential of the solution (Levett et al., 2020). Aluminum

622 migrated as a soluble cation due to changes in solution pH and/or organic chemistry,
623 resulting in the observed depletion of aluminum and the relative concentrations of
624 titanium and iron in the topsoil (Ramanaidou, 2009). The Dali topsoil has notably
625 higher $\text{TiO}_2/\text{Al}_2\text{O}_3$ (0.195-0.198) compared to Layers 2, 3, and 4 (0.103-0.132) (Table
626 3), suggesting that depletion of aluminum may have occurred during the weathering
627 process.

628

629 **5. Conclusions**

630 The distribution of authigenic minerals in the Dali basalt-derived soil is largely
631 defined by soil layers related to pedogenesis. Smectite decreases upward from 39-64%
632 in Layer 4 to 12% in the topsoil, whereas I/S and K/S increase upward from 0-2% to
633 24% and from 36-59% to 64%, respectively. Clay phases from the saprolite have a
634 mixture of di- and trioctahedral species, whereas those from the middle to upper soil
635 profile have a uniformly dioctahedral structure. I/S clays are characterized by
636 interstratification of 12-Å smectite with 10-Å illite layers, whereas K/S clays exhibit
637 intercalation of 12-Å smectite and 7-Å kaolinite layers. The intercalation of 12-, 10-,
638 and 7-Å clay layers represents mixed-layer I/S/K clays. The significantly greater
639 abundance of K/S clay relative to I/S clay in the saprolite implies that kaolinization of
640 smectite took place at an early stage after smectite formation, whereas illitization of
641 smectite occurred during a later stage characterized by increased leaching. However,
642 the processes of kaolinization and illitization of smectite overlapped during the
643 developmental history of the soil.

644 Desilication and K-fixation of smectite occurred with advanced weathering, but the
645 absence of discrete kaolinite and illite and the lack of detectable gibbsite in the soils
646 indicate that the Dali soils formed in a weathering environment of only moderate
647 intensity. Both the immobile oxides (TFe_2O_3 and TiO_2) and a mobile component (K_2O)
648 are markedly concentrated in the topsoil. The concentration of K in the weathering
649 profile was potentially related to incorporation of K in the interlayer of illite due to
650 smectite illitization in response to more advanced weathering and pedogenic
651 processes, and the relative accumulation of K in the topsoil probably results from
652 fertilizer in land use and recycling of K by plants.

653

654 **Acknowledgments**

655 This work was supported by the National Natural Science Foundation of China
656 (Projects 41972040, 42172045, and 42002042), the Fundamental Research Funds for
657 the Central Universities, China University of Geosciences (Wuhan) (No.
658 CUG170106), and the Postdoctoral Science Foundation of China (2020M672440).
659 The authors also wish to thank Dr. Fan Li for assistance in sample collection, and
660 especially Dr. Fabio Scarciglia, the handling editor, and two anonymous reviewers for
661 their insightful reviews, valuable comments, and suggestions.

662

663 **References**

- 664 Alexander, G.C., Heal, H.G., 1974. Ion-exchange properties and possible applications
665 of weathered Antrim basalts. *Journal of Chemical Technology and Biotechnology*
666 24, 387–400.
- 667 Arslan, M., Kadir, S., Abdioglu, E., Kolayli, H., 2006. Origin and formation of kaolin
668 minerals in saprolite of Tertiary alkaline volcanic rocks, Eastern Pontides, NE
669 Turkey. *Clay Minerals* 41, 597–617.
- 670 Babechuk, M.G., Widdowson, M., Kamber, B.S., 2014. Quantifying chemical

671 weathering intensity and trace element release from two contrasting basalt profiles,
672 Deccan Traps, India. *Chemical Geology* 363, 56–75.

673 Bain, D.C., Ritchie, P.F.S., Clark, D.R., Duthie, D.M.L., 1980. Geochemistry and
674 mineralogy of weathered basalt from Morvern, Scotland. *Mineralogical Magazine*
675 43, 865–872.

676 Bakker, E., Lanson, B., Findling, N., Wander, M.M., Hubert, F., 2019. Mineralogical
677 differences in a temperate cultivated soil arising from different agronomic
678 processes and plant K-uptake. *Geoderma* 347, 210–219.

679 Bakker, L., Lowe, D.J., Jongmans, A.G., 1996. A micromorphological study of
680 pedogenic processes in an evolutionary soil sequence formed on Late Quaternary
681 rhyolitic tephra deposits, North Island, New Zealand. *Quaternary International*
682 34-36, 249–261.

683 Barbera, V., Raimondi, S., Egli, M., Plotze, M., 2008. The influence of weathering
684 processes Mediterranean on labile and stable organic matter in volcanic soils.
685 *Geoderma* 143, 191–205.

686 Barré, P., Velde, B., Abbadie, L., 2007. Dynamic role of “illite-like” clay minerals in
687 temperate soils: facts and hypotheses. *Biogeochemistry* 82, 77–88.

688 Berry, L.G., Mason, B., Dietrich, R.V., 1983. *Mineralogy–Concepts, Descriptions,*
689 *Determinations.* W. H. Freeman and Company, San Francisco, 561 pp.

690 Brantley, S.L., Goldhaber, M., Ragnarsdottir, K.V., 2007. Crossing disciplines and
691 scales to understand the critical zone. *Elements* 3, 307–314.

692 Campodonico, V.A., Pasquini, A.I., Lecomte, K.L., García, M.G., Depetris, P.J., 2019.
693 Chemical weathering in subtropical basalt-derived laterites: A mass balance
694 interpretation (Misiones, NE Argentina). *Catena* 173, 352–366.

695 Caner, L., Radtke, L.M., Vignol-Lelarge, M.L., Inda, A.V., Bortoluzzi, E.C., Mexias,
696 A.S., 2014. Basalt and rhyo-dacite weathering and soil clay formation under
697 subtropical climate in southern Brazil. *Geoderma* 235–236, 100–112.

698 Chen, J.M., Gong, G., Zhao, L.Q., Sun, X.C., 2000. Determination of cation exchange
699 capacity of expansive soils. *Rock and Mineral Analysis* 19 (2), 152–154 (in
700 Chinese with English abstract).

701 Cheng, F., Hong, H.L., Bae, C.J., Li, Z., Algeo, T.J., Huang, S.M., Cheng, L.L., Fang,
702 Q., 2018. Geochemical and detrital zircon U-Pb geochronological constraints on
703 provenance of the Xiaomei red earth sediments (Bose Basin, Guangxi Province,
704 southern China). *Palaeogeography, Palaeoclimatology, Palaeoecology* 2018, 510,
705 49–62.

706 Cheng, S., Hong, H.L., Ji, K.P., Li, F., Wang, X.H., 2022. New insight into biotite
707 weathering in the subtropic Tongcheng granite regolith, Hubei Province, South
708 China. *Applied Clay Science* 224, 106518.

709 Chesworth, W., 1973. The parent rock effect in the genesis of soil. *Geoderma* 10,
710 215–225.

711 Chesworth, W., Duou, J., Larroque, P., 1981. The weathering of basalt and relative
712 mobilities of the major elements at Belbex, France. *Geochimica et Cosmochimica*
713 *Acta* 45, 1235–1243.

714 Christidis, G.E., 1998. Comparative study of the mobility of major and trace elements
715 during alteration of an andesite and a rhyolite to bentonite, in the islands of Milos
716 and Kimolos, Aegean, Greece. *Clays and Clay Minerals* 46, 379–399.

717 Courtillot, V., Jaupart, C., Manighetti, I., Tapponnier, P., Besse, J., 1999. On causal
718 links between flood basalts and continental breakup. *Earth and Planetary Science*
719 *Letters* 166, 177–195.

720 Curi, N., Franzmeier, D.P., 1987. Effect of parent rocks on chemical and
721 mineralogical properties of some Oxisols in Brazil. *Soil Science Society of*
722 *America Journal* 51, 153–158.

723 Curtin, D., Smillie, G.W., 1981. Composition and origin of smectite in soils derived
724 from basalt in Northern Ireland. *Clays and Clay Minerals* 29, 277–284.

725 Daux, V., Crovisier, J.L., Hemond, C., Petit, J.C., 1994. Geochemical evolution of
726 basaltic rocks subjected to weathering: fate of the major elements, rare earth
727 elements, and thorium. *Geochimica et Cosmochimica Acta* 58, 4941–4954.

728 De Rosa, R., Donato, P., Scarciglia, F., 2016. On the origin and post-depositional
729 history of widespread massive ash deposits: The case of Intermediate Brown Tuffs
730 (IBT) of Lipari (Aeolian Islands, Italy). *Journal of Volcanology and Geothermal*

731 Research 327, 135–151.

732 Deepthy, R., Balakrishnan, S., 2005. Climatic control on clay mineral formation:
733 evidence from weathering profiles developed on either side of the Western Ghats.
734 *Journal of Earth System Science* 114, 545–556.

735 Dekayir, A., El-Maataoui, M., 2001. Mineralogy and geochemistry of supergene
736 alteration of an alkali basalt from the Middle Atlas, Morocco. *Journal of African*
737 *Earth Sciences* 32, 619–633.

738 Eggleton, R.A., Foudoulis, C., Varkevisser, D., 1987. Weathering of basalt: changes in
739 rock chemistry and mineralogy. *Clays and Clay Minerals* 35, 161–169.

740 Glassmann, J.R., Simonson, G.M., 1985. Alteration of basalt in soils of Western
741 Oregon. *Soil Science Society of America Journal* 49, 262–273.

742 He, B., Xu, Y.G., Xiao, L., Wang, K.M., Sha, S.L., 2003. Generation and spatial
743 distribution of the Emeishan Large Igneous Province: New evidence from
744 stratigraphic records. *Acta Geologica Sinica* 77, 194–201 (in Chinese with English
745 abstract).

746 He, Y., Li, D.C., Velde, B., Yang, Y.F., Huang, C.M., Gong, Z.T., Zhang, G.L., 2008.
747 Clay minerals in a soil chronosequence derived from basalt on Hainan Island,
748 China and its implication for pedogenesis. *Geoderma* 148, 206–212.

749 Hillier, S., 2000. Accurate quantitative analysis of clay and other minerals in
750 sandstones by XRD: comparison of a Rietveld and a reference intensity ratio (RIR)
751 method and the importance of sample preparation. *Clay Minerals* 35, 291–302.

752 Hong, H.L., Zhang, N., Li, Z., Xue, H.J., Xia, W.C., Yu, N., 2008. Clay mineralogy
753 across the P/T boundary of the Xiakou section, China: evidence of clay provenance
754 and environment. *Clays and Clay Minerals* 56, 131–143.

755 Hong, H.L., Churchman, G.J., Gu, Y.S., Yin, K., Wang, C.W., 2012. Kaolinite–
756 smectite mixed-layer clays in the Jiujiang red soils and their climate significance.
757 *Geoderma* 173–174, 75–83.

758 Hong, H.L., Fang, Q., Wang, C.W., Churchman, G.J., Zhao, L.L., Gong, N.N., Yin, K.,
759 2017. Clay mineralogy of altered tephra beds and facies correlation between the
760 Permian-Triassic boundary stratigraphic sets, Guizhou, South China. *Applied Clay*

761 Science 143, 10–21.

762 Hong, H.L., Algeo, T.J., Fang, Q., Zhao, L.L., Ji, K.P., Yin, K., Wang, C.W., Cheng,
763 S.L., 2019. Facies dependence of the mineralogy and geochemistry of altered
764 volcanic ash beds: An example from Permian-Triassic transition strata in
765 southwestern China. *Earth-Science Reviews* 190, 58–88.

766 Hou, Z.Q., Lu, J.R., Wang, Y.L., Xia, L.Q., Li, H.Y., Guo, L.J., 1999. Emei large
767 igneous province: characteristics and origin. *Geological Review* 45 (Supp.), 885–
768 891 (in Chinese with English abstract).

769 Inoue, A., Utada, M., 1991. Pumpellyite and related minerals from hydrothermally
770 altered rocks at the Kalmikta area, northern Honshu, Japan. *The Canadian*
771 *Mineralogist* 29, 255–270.

772 Jackson, M.L., 1978. *Soil Chemical Analysis*. Self-Published, University of
773 Wisconsin, Madison, U.S.A.

774 Jeong, G.Y., Kim, H.B., 2003. Mineralogy, chemistry, and formation of oxidized
775 biotite in the weathering profile of granitic rocks. *American Mineralogist* 88, 352–
776 364.

777 Jiang, K., Qi, H.W., Hu, R.Z., 2018. Element mobilization and redistribution under
778 extreme tropical weathering of basalts from the Hainan Island, South China.
779 *Journal of Asian Earth Sciences* 158, 80–102.

780 Kantor, W., Schwertmann, U., 1974. Mineralogy and genesis of clays in red-black
781 toposequences in Kenya. *Journal of Soil Science* 25, 67–78.

782 Kittrick, J.A., 1973. Mica-derived vermiculites as unstable intermediates. *Clays and*
783 *Clay Minerals* 21, 479–488.

784 Lessovaia, S.N., Plötze, M., Inozemzev, S., Goryachkin, S., 2016. Traprock
785 transformation into clayey materials in soil environments of the Central Siberian
786 Plateau, Russia. *Clays and Clay Minerals* 64, 668–676.

787 Levett, A., Vasconcelos, P.M., Gagen, E.J., Rintoul, L., Spier, C., Guagliardo, P.,
788 Southam, G., 2020. Microbial weathering signatures in lateritic ferruginous
789 duricrusts. *Earth and Planetary Science Letters* 538, 116209.

790 Li, G.J., Hartmann, J., Derry, L.A., West, A.J., You, C.F., Long, X.Y., Zhan, T., Li,

791 L.F., Li, G., Qiu, W.H., Li, T., Liu, L.W., Chen, Y., Ji, J.F., Zhao, L., Chen, J., 2016.
792 Temperature dependence of basalt weathering. *Earth and Planetary Science Letters*
793 443, 59–69.

794 Liivamägi, S., Šrodoň, J., Bojanowski, M.J., Gerdes, A., Stanek, J.J., Williams, L.,
795 Szczerba, M., 2018. Paleosols on the Ediacaran basalts of the East European Craton:
796 A unique record of paleoweathering with minimum diagenetic overprint.
797 *Precambrian Research* 316, 66–82.

798 Ma, Y.J., Luo, J.X., Jiang, M.Y., Yang, D.Y., 1999. The weathering and evolution of
799 soil ferrallite minerals in the South China. *Acta Sedimentologica Sinica*, 17 (Supp.),
800 681-686 (in Chinese text with English abstract).

801 Markússon, S.H., Stefánsson, A., 2011. Geothermal surface alteration of basalts,
802 Krýsuvík Iceland—Alteration mineralogy, water chemistry and the effects of acid
803 supply on the alteration process. *Journal of Volcanology and Geothermal Research*
804 206, 46–59.

805 Mavris, C., Ploetze, M., Mirabella, A., Giaccai, D., Valboa, G., Egli, M., 2011. Clay
806 mineral evolution along a soil chronosequence in an Alpine proglacial area.
807 *Geoderma* 165, 106–117.

808 Mevel, C. 1981. Occurrence of pumpellyite in hydrothermally altered basalts from the
809 Vema fracture zone (mid-Atlantic ridge). *Contributions to Mineralogy and*
810 *Petrology* 76, 386–393.

811 Mirabellal, A., Egli, M., Raimondi, S., Giaccai, D., 2005. Origin of clay minerals in
812 soils on pyroclastic deposits in the island of Lipari (Italy). *Clays and Clay Minerals*
813 53, 409–421.

814 Nesbitt, H.W., 1979. Mobility and fractionation of rare earth elements during
815 weathering of a granodiorite. *Nature* 279, 206–210.

816 Nesbitt, H.W., Wilson, R.E., 1992. Recent chemical weathering of basalts. *American*
817 *Journal of Science* 292, 740–777.

818 Orhan, D., Hüseyin, S., 2018. Effect of toposequences on geochemical mass balance
819 and clay mineral formation in soils developed on basalt parent material under
820 subhumid climate condition. *Indian Journal of Geo-Marine Sciences* 47, 1809–

821 1820.

822 Perez-Fodich, A., Derry, L.A., 2019. Organic acids and high soil CO₂ drive intense
823 chemical weathering of Hawaiian basalts: Insights from reactive transport models.
824 *Geochimica et Cosmochimica Acta* 249, 173–198.

825 Pokrovsky, O.S., Schott, J., Kudryavtzev, D.I., Dupre, B., 2005. Basalt weathering in
826 Central Siberia under permafrost conditions. *Geochimica et Cosmochimica Acta* 69,
827 5659–5680.

828 Prudêncio, M.I., Sequeira Braga, M.A., Paquet, H., Waerenborgh, J.C., Pereira, L.C.J.,
829 Gouveia, M.A., 2002. Clay mineral assemblages in weathered basalt profiles from
830 central and southern Portugal: climatic significance. *Catena* 49, 77– 89.

831 Qiao, Y., Hao, Q., Peng, S., Wang, Y., Li, J., Liu, Z., 2011. Geochemical
832 characteristics of the eolian deposits in southern China, and their implications for
833 provenance and weathering intensity. *Palaeogeography, Palaeoclimatology,*
834 *Palaeoecology* 308, 513–523.

835 Ramanaidou, E.R., 2009. Genesis of lateritic iron ore from banded iron-formation in
836 the Capanema mine (Minas Gerais, Brazil). *Australian Journal of Earth Sciences* 56,
837 605–620.

838 Rasmussen, C., Dahlgren, R.A., Southard, R.J., 2010. Basalt weathering and
839 pedogenesis across an environmental gradient in the southern Cascade Range,
840 California, USA. *Geoderma* 154, 473–485.

841 Reynolds, R.C., Jr., Reynolds, R.C., III, 1996. *NEWMOD-for-Windows. The*
842 *Calculation of One-dimensional X-ray Diffraction Patterns of Mixed-layered Clay*
843 *Minerals.* Hanover, New Hampshire.

844 Righi, D., Terribile, F. and Petit, S., 1999. Pedogenic formation of kaolinite-smectite
845 mixed layers in a soil toposequence developed from basaltic parent material in
846 Sardinia (Italy). *Clays and Clay Minerals* 47, 505–514.

847 Ryan, P.C., Huertas, F.J., 2009. The temporal evolution of pedogenic Fe–smectite to
848 Fe–kaolin via interstratified kaolin–smectite in a moist tropical soil chronosequence.
849 *Geoderma* 151, 1–15.

850 Sheldon, N.D., 2003. Pedogenesis and geochemical alteration of the Picture Gorge

851 subgroup, Columbia River basalt, Oregon. *Geological Society of America Bulletin*
852 115, 1377–1387.

853 Singer, A., Ármannsson, H., 1999. Weathering of basic magmatic rocks under
854 Mediterranean conditions. *Geochemistry of the Earth's Surface International*
855 *Symposium*, 1999.

856 Sulieman, M.M., Sh Sallam, A., Brevik, E.C., Al-farraaj, A.S., 2020. Investigation of
857 the clay minerals composition of soils derived from basalt parent materials in the
858 Early Miocene to Early Pleistocene on the Arabian Shield using multiple
859 techniques: implications for paleoclimatic conditions. *Environmental Earth*
860 *Sciences* 79, Article number: 297.

861 Van Der Gaast, S.J., Mizota, C., and Jansen, J.H.F. (1986) Curved smectite in soils
862 from volcanic ash in Kenya and Tanzania: A low-angle X-ray powder diffraction
863 study. *Clays and Clay Minerals* 34, 665–671.

864 Van Ranst, V., Kips, P., Mbogoni, J., Mees, F., Dumon, M., Delvaux, B., 2020.
865 Halloysite-smectite mixed-layered clay in fluvio-volcanic soils at the southern foot
866 of Mount Kilimanjaro, Tanzania. *Geoderma* 375, 114527.

867 Vingiani, S., Righi, D., Petit, S., Terribile, F., 2004. Mixed-layer kaolinite-smectite
868 minerals in a red-black soil sequence from basalt in Sardinia (Italy). *Clays and Clay*
869 *Minerals* 52, 473–483.

870 Voicu, G., Bardoux, M., Voicu, D., 1997. Mineralogical norm calculations applied to
871 tropical weathering profiles. *Mineralogical Magazine* 61, 185–196.

872 Wang, R.Z., Yang, J.J., Liu, H.Y., Sardans, J., Zhang, Y.H., Wang, X.B., Wei, C.Z., Lu,
873 X.T., Dijkstra, F.A., Jiang, Y., Han, X.G., Penuelas, J., 2022. Nitrogen enrichment
874 buffers phosphorus limitation by mobilizing mineral-bound soil phosphorus in
875 grasslands. *Ecology* 103, e3616.

876 Wilson, S.G., Lambert. J.J., Nanzyo, M., Dahlgren, R.A., 2017. Soil genesis and
877 mineralogy across a volcanic lithosequence. *Geoderma* 285, 301–312.

878 Ziegler, K., Hsieh, J.C.C., Chadwick, O.A., Kelly, E.F., Hendricks, D.M., Savin, S.M.,
879 2003. Halloysite as a kinetically controlled end product of arid-zone basalt
880 weathering. *Chemical Geology* 202, 461– 478.